

Analysis of the X-ray and time-resolved XUV emission of laser produced Xe and Kr plasmas

S. Bastiani-Ceccotti^{a,*}, N. Kontogiannopoulos^a, J.-R. Marquès^a, S. Tzortzakis^a,
L. Lecherbourg^a, F. Thais^b, I. Matsushima^c, O. Peyrusse^d, C. Chenais-Popovics^a

^a *Laboratoire pour l'Utilisation des Lasers Intenses (LULI), Ecole Polytechnique, CNRS, CEA, UPMC; Route de Saclay, 91128 Palaiseau, France*

^b *CEA/DSM/SPAM, Centre d'Etudes de Saclay, 91191 Gif-sur-Yvette Cedex, France*

^c *National Institute of Advanced Industrial Science and Technology, Tsukuba 3058568, Japan*

^d *CELIA, UMR 5107 Université Bordeaux I-CEA-CNRS, 33405 Talence, France*

Available online 4 February 2007

Abstract

A frequency-doubled laser beam of the Nd:glass kilojoule nanosecond LULI2000 facility (1.5 ns duration, 200–400 J energy, 0.53 μm wavelength) was focused on a Xe or Kr gas jet. The plasma was simultaneously diagnosed with X-ray (in the wavelength range of 6–8 \AA for Kr and of 12–15 \AA for Xe) and time-resolved XUV (20–200 \AA) emission spectroscopy. Electron density and temperature as well as the ionization charge were measured by time-resolved Thomson scattering of the heating laser pulse. The spectra are compared with the calculations performed with the NLTE collisional-radiative code AVERROES/TRANSPEC. Best fits of the X-ray and XUV spectra obtained are presented. The measured charge distribution and dynamics is analyzed using the simultaneous Thomson scattering diagnostic.

© 2007 Elsevier B.V. All rights reserved.

PACS: 52.50.Jm; 52.25.Os; 32.70.Fw; 52.70.La

Keywords: Plasma spectroscopy; Non-LTE plasmas; High-Z plasmas; L-shell spectra; M-shell spectra; XUV emission

1. Introduction

Multicharged ions are present in hot dense plasmas and play a major role in radiation transport in stellar atmospheres and in inertial confinement fusion plasmas. High atomic number Z , multi-charged ion plasmas are also ideal for the production of bright X-ray sources. These high- Z plasmas are usually not in local-thermodynamic-equilibrium (NLTE) and are described by complex atomic physics models, which are the subject of much research and numerous discussions [1,2]. The primary reason is that calculation of complete spectra of high- Z elements by traditional detailed atomic structure codes coupled to population kinetics models incorporating several ions requires an unmanageably large number of transitions

and energy levels. Thus, statistical approaches involving groupings of levels, e.g., configurations [3] and superconfigurations [4,5], prove to be very efficient when combined with the Unresolved Transition Array (UTA/SOSA) formalism [6] and/or the SuperTransition Array (STA) formalism [7]. Further, there are recent efforts to develop hybrid calculations mixing detailed levels and configurations [8,9]. In addition to, and in support of, the theoretical effort there is a need for experimental benchmarks from measurements of well-diagnosed plasmas [10–14].

In the present experiment, we attempt to create quasi-homogeneous, quasi steady-state, large scale (millimeter size) plasmas by focusing a nanosecond laser pulse into a gas jet. Both time-integrated X-ray and time-resolved XUV spectra emitted by plasmas of xenon and krypton were recorded. The Thomson scattering diagnostic provided the mean electron temperature and density of the plasma, and its average charge. In contrast to the previous studies performed with

* Corresponding author.

E-mail address: serena.bastiani@polytechnique.fr (S. Bastiani-Ceccotti).

the LULI facility [12–15], the simultaneous measurement of time-resolved XUV spectra is implemented here, and krypton spectra have been measured. Calculations performed with the AVERROES/TRANSPPEC NLTE collisional-radiative super-configuration code [5] are compared with experimental results.

2. Experimental setup

The experiment was performed on the LULI2000 facility where we focused a flat-top, 1.5 ns duration, frequency-doubled neodymium laser beam ($\lambda = 0.53 \mu\text{m}$) on a Xe ($Z = 54$) or Kr ($Z = 36$) gas jet, with a $f = 800$ mm lens coupled to a random phase plate (RPP) to obtain an elliptic focal spot of 1 mm (horizontal) \times 150 μm (vertical) size, measured between the zeros of the intensity distribution function. The laser energy was varied from 100 to 400 J, corresponding to intensities from 0.5 to 2×10^{14} W/cm², respectively. The laser was focused at a distance of 750 μm from the exit plane of a 1 mm diameter supersonic gas nozzle. At this distance, the radial density profile of the gas jet, measured by Mach-Zehnder interferometry, has a super-Gaussian-like shape, with a 0.25 mm gradient at its border, followed by a 1 mm diameter homogeneous plateau. The horizontal width of the focal spot has been chosen to match the 1 mm diameter to minimize the reabsorption effects of a surrounding cold gas layer. On the other hand, the vertical size of the focal spot was chosen to minimize the effect of source broadening, so to optimize the spectral resolution of the Bragg crystal spectrograph. The gas jet backing pressure was varied from 1.3 to 7.0 bar, giving an ion density in the focal volume varying linearly with the pressure from 1.7 to 9.0×10^{18} cm⁻³.

The laser energy absorption by the plasma was measured with a calorimeter set in front of the incident beam. The calorimeter was calibrated by measuring the beam energy without the gas jet, i.e. without absorption. The laser absorption increased from 28% to 55% when the gas pressure was varied from 1.3 to 7 bar. The laser–gas interaction region was monitored with an X-ray pinhole camera. We simultaneously recorded the time-integrated X-ray spectra in the keV range and the time-resolved XUV spectra emitted from the plasma at 90° from the laser axis. In previous experiments, it was demonstrated that the keV X-ray photons are emitted during the laser pulse and that the spectral shape of the emission remains almost the same for the duration of the laser pulse [12]. So, we measured the time-integrated keV emission with a double Bragg crystal spectrograph, composed by a TIAP crystal and an ADP crystal. The TIAP crystal recorded the 3d–4f transitions of xenon, in the 12–15 Å range, and the ADP crystal covered the 2–3 and 2–4 transitions of krypton, in the 6–8 Å range. The spectral resolution was 38 mÅ and 16 mÅ for the Xe and Kr spectra, which was limited by the 150 μm height of the laser focal spot, respectively. A vertical, 200 μm width slit in front of each crystal yielded a 330 μm spatial resolution along the laser axis. The spectra were registered on Kodak DEF films. Unlike the X-ray spectral measurement, time resolution is required to measure the XUV emission. Indeed, we previously observed that the XUV

spectra have a strong time dependence as the plasma emits during the recombination phase that occurs after the laser pulse [13]. For gas jet experiments the use of a streak camera is complicated by the need for protection from the sudden pressure increase when the gas jet is triggered. To circumvent this we implemented a differential pumping system through a 500 μm width slit. The XUV spectra were measured in the 20–200 Å range with a 2000 l/mm transmission grating coupled to a 5.2 m radius spherical imaging nickel mirror. The resolution of the spectrograph was 2.5 Å, and the time resolution of the camera was around 50 ps.

The plasma electron density and temperature were obtained by the analysis of the Thomson self-scattering signal. The incident laser beam, backscattered at 135° from the laser propagation direction, was collected with a $f/6$ lens and relayed to two spectrometers coupled to streak cameras with temporal resolution better than 20 ps, one with a high (0.2 nm) spectral resolution to resolve the ionic component, and the other with a lower resolution (6.4 nm) to record the full electron component. The observed volume, defined by the collecting lens aperture and by the spectrometer and streak camera slits, was 50(height) \times 200(width) \times 300(depth) μm^3 , and thus probed the heated plasma volume. Comparison between measured and theoretical spectra permits one to infer (i) the value of the product of the average charge by the electronic temperature ZT_e , from the ionic component, (ii) the electron density n_e from the electron component [16]. A few Mach-Zehnder interferometry measurements were performed with helium gas to determine the ion density at a given backing pressure, irrespectively of the nature of the gas.

3. Experimental results

3.1. Thomson self-scattering diagnostic

An example of the Thomson scattering raw data for xenon at 2 bar backing pressure and 120 J laser energy is displayed in Fig. 1a and b for the time-resolved ion and electron features. For the ion feature spectrum, we see the two satellites on both sides of the laser wavelength. The wavelength separation between the satellites is proportional to the ion sound velocity:

$$c_s \approx \sqrt{\frac{ZT_e}{m_i} \left(\frac{1}{1 + (k\lambda_D)^2} + \frac{3T_i}{ZT_e} \right)}$$

where m_i is the ion mass, k the plasma perturbation wavenumber, λ_D the Debye length, and T_i the ionic temperature. In our experiment, the plasma and the diffusion geometry are such that $k\lambda_D < 1$ and $T_i \ll ZT_e$, then the separation is mainly dependent on ZT_e . Fig. 1a shows that the separation increases very rapidly (as ionization and temperature increase), with a rise time similar to that of the laser pulse (about 0.2 ns), and then remains constant during the laser pulse duration. For all the experiments we observed that the red satellite is brighter than the blue one. This can be explained by the presence of

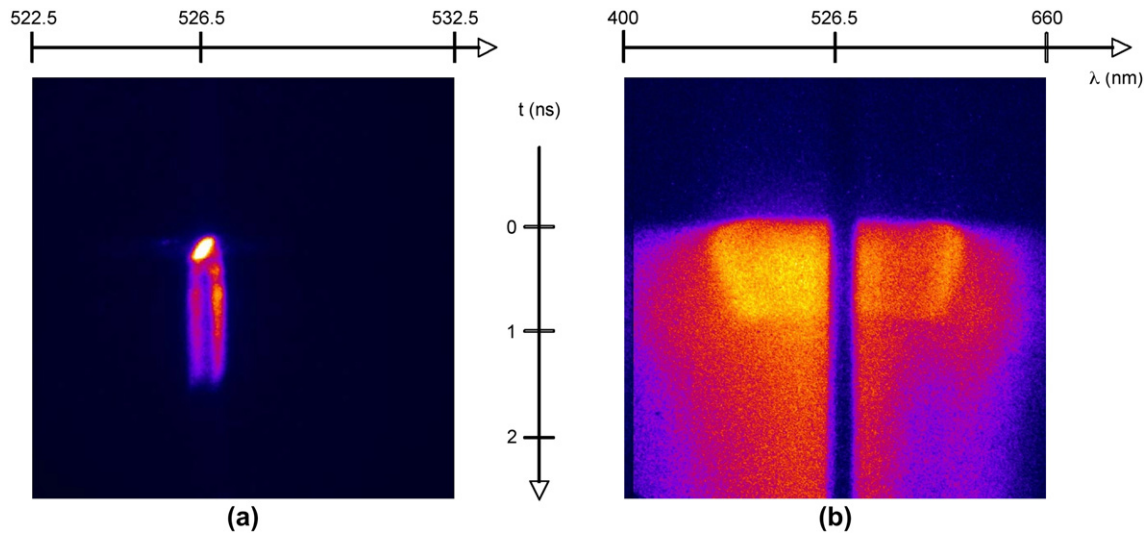


Fig. 1. Thomson self-scattering spectra measured on xenon (2 bar, 120 J). (a) Ionic satellites; (b) electronic satellites (the dark region in the middle of the spectrum corresponds to the ion component attenuated by an interference filter).

a Brillouin instability, or by a velocity drift of the electrons with respect to the ions (estimated to about 10^4 m/s).

On the electron feature spectrum, the dark region in the middle of the spectrum is centered on the laser wavelength and corresponds to the ion component, which is strongly attenuated by an interference filter placed at the spectrometer entrance. The separation between the maxima on both sides of this central region is proportional to the Bohm–Gross frequency:

$$\omega_{\text{BG}} = \omega_{\text{pe}} \sqrt{1 + 3(k\lambda_{\text{D}})^2}$$

where ω_{pe} is the electron plasma frequency. One can see in Fig. 1b that at the beginning of the signal, the edges of the electron feature satellites separate very rapidly due to the rapid ionization of the plasma. Later in time, this separation slowly decreases due to a slow reduction of electron density. This reduction is typically of the order of $10^{19} \text{ cm}^{-3}/\text{ns}$, in good agreement with the expansion by thermal pressure. As several additional mechanisms modify the maximum and width of the satellites, the analysis of these spectra was performed with

a parametric fit of the measured spectra using theoretical plots [13]. The experiments obtained for different laser energies and gas pressures of Xe and Kr gave the following parameters: $n_e = 0.2\text{--}1.2 \times 10^{19} \text{ cm}^{-3}$, $Z = 12\text{--}24$, $T_e = 160\text{--}500 \text{ eV}$.

3.2. XUV spectroscopy

Typical streak camera images of the time-resolved XUV emission of xenon and krypton are shown in Fig. 2, for a gas pressure of 4 bar and a laser energy around 360 J. The wavelengths were calibrated using the Be filter K-edge and Al filter L-edge. The origin of the wavelength axis is the zero order of the grating. It is immediately obvious that the emission lasts longer than the 1.5 ns laser pulse. The time dependence is especially visible around 50 \AA for xenon, where a bright structure disappears earlier than the rest of the spectrum. Previous calculations had shown that the xenon Co-like ions (Xe^{27+}) emit around 50 \AA [15]. So, the present result shows that this highly ionized charge state disappears after about 1 ns. For krypton, the structures observed below 50 \AA disappear at around 2 ns, i.e., more quickly than the rest of

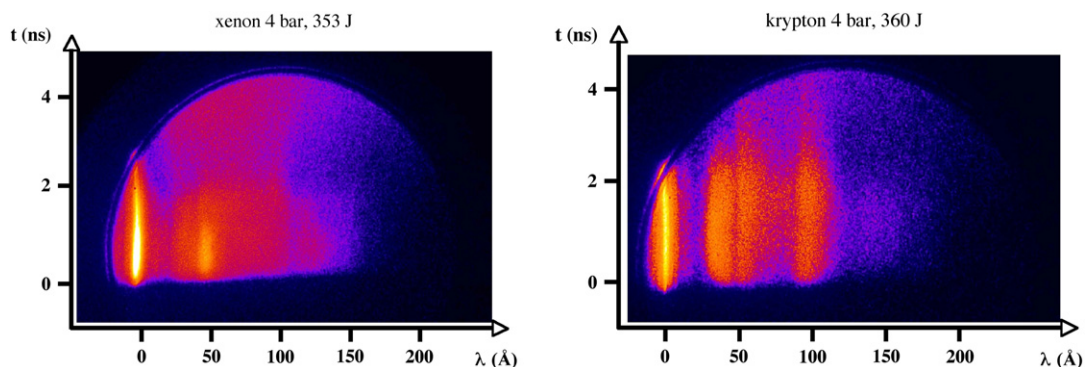


Fig. 2. XUV streaked images recorded for xenon and krypton at 4 bar gas pressure and about 360 J laser energy.

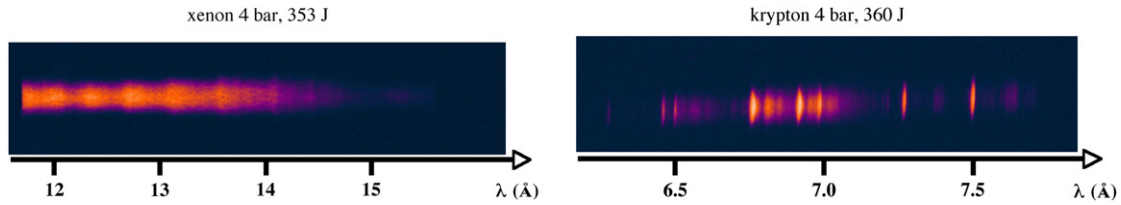


Fig. 3. Raw X-ray images recorded for xenon and krypton at 4 bar gas pressure and about 360 J laser energy. The vertical axis is the plasma image along the laser axis.

the spectrum. This behavior is expected, as the recombining plasma emits at lower photon energies.

3.3. keV X-ray spectroscopy

An example of the raw spectra obtained with the X-ray spectrograph is shown in Fig. 3, for same condition as shown in Fig. 2. We observe that the plasma is quite homogeneous in the laser propagation direction (vertical axis on the images). In Fig. 4 we present the lineouts of the X-ray spectra obtained at the center of the gas jet for different gas pressures and laser energies. The xenon spectrum is composed of 3d-4f Unresolved Transition Arrays emitted by different ion stages from Ni-like (Xe^{26+}) to V-like (Xe^{31+}). For krypton, the spectrum is dominated by the $n=2-3$ and $n=2-4$ transitions from Na-like (Kr^{25+}) to F-like (Kr^{27+}). For both elements one observes that the transition arrays intensity ratios follow the ionization, which increases with incident laser intensity and gas pressure, that are directly related to absorbed energy. The dependence with Kr gas pressure on the F-/Ne-like intensity ratios is especially clear in the 6.4–6.7 Å spectral range. For Xe, the spectra measured for 2 bar – 127 J and 1.3 bar – 420 J are very similar, showing that the absorbed laser energy is similar for these two different conditions. Further, the spectrum obtained for Xe, for 1.3 bar pressure and 420 J energy is very similar to the results of previous experiments [12]. It is important to note that there is a disagreement between the Z inferred from Thomson

scattering and that extracted from the observed emission. This point is discussed further below in the text.

4. AVERROES/TRANSPEC calculations

We compare the measured XUV and X-ray spectra to *ab initio* calculations performed with the AVERROES/TRANSPEC (A/T) superconfiguration code [5]. AVERROES first calculates the collisional and radiative rates, and the superconfiguration energies. Second, these data are used in the collisional-radiative model TRANSPEC, which computes NLTE populations and generates synthetic spectra using given ion density and electron temperature. These parameters are provided, ideally, by the Thomson scattering (TS) diagnostic. To calculate the time evolution of the XUV emission, we assume a temporal profile for the electron temperature characterized by a fast rise, 0.2 ns, followed by a 0.25 ns duration plateau at the TS deduced value for the temperature, and then followed by a relatively slow decay, giving a total duration of 4.5 ns.

4.1. Xenon spectra

A typical result for the xenon case is plotted in Fig. 5. The dashed lines are the XUV spectra measured at different times during the plasma expansion, for an experiment having 2 bar backing pressure and 355 J laser energy. The spectra are then compared to the calculation from the A/T code, obtained with

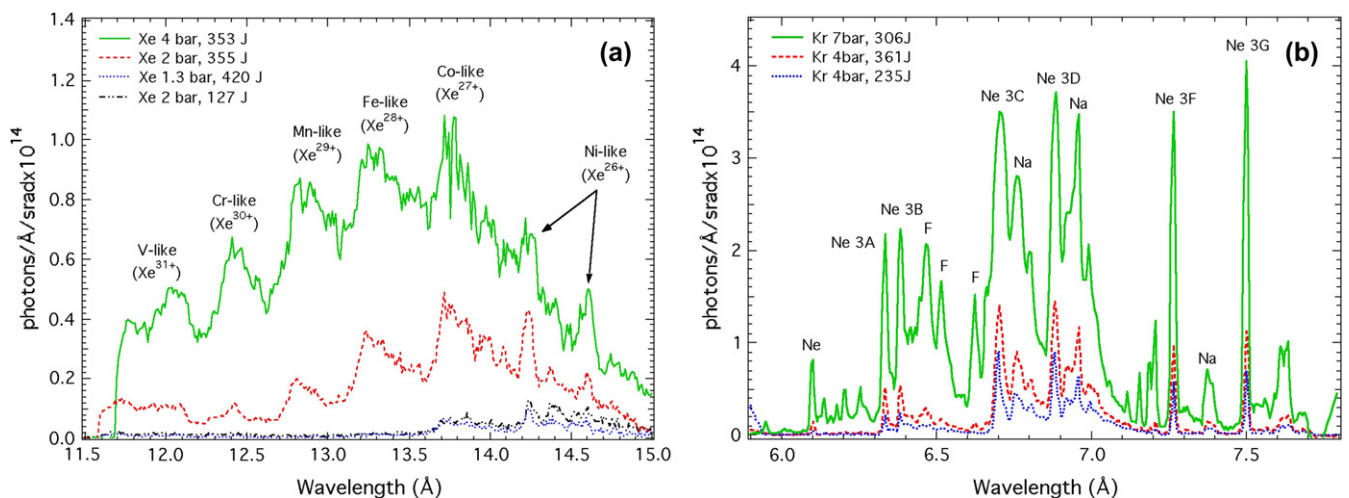


Fig. 4. X-ray spectra traced at the center of the gas jet, as a function of gas pressure and laser energy. (a) Xenon, and (b) krypton.

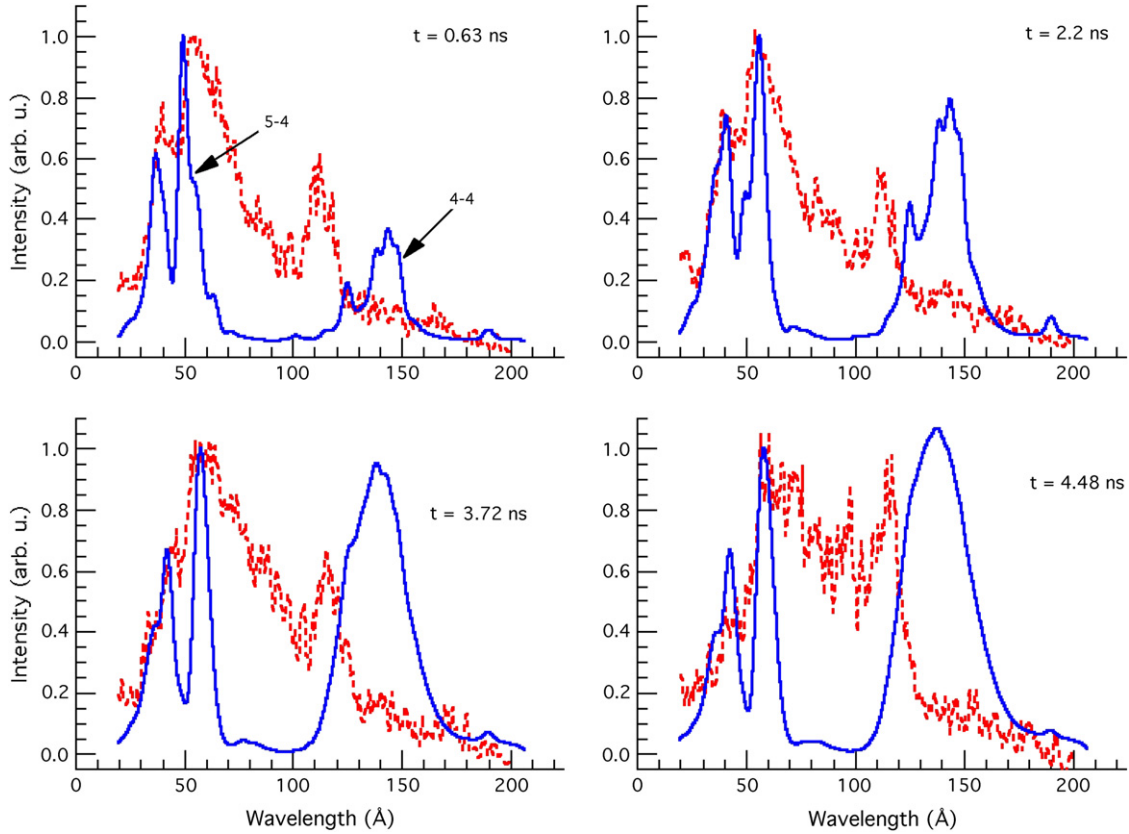


Fig. 5. Xenon XUV spectra recorded at different times, for 2 bar gas pressure and 355 J laser energy (dashed lines). The AVERROES calculations (full lines) are performed with the plasma parameters deduced by the TS diagnostic ($N_i = 2.57 \times 10^{18} \text{ cm}^{-3}$ and $T_e = 330 \text{ eV}$).

the TS deduced values for this shot ($N_i = 2.57 \times 10^{18} \text{ cm}^{-3}$ and $T_e = 330 \text{ eV}$). We observe that the agreement is better for the short wavelength part of the spectra. The relative intensity of the two 5–4 structures is well reproduced, although the width is underestimated. The situation is problematic on the long wavelength side of the spectra, where the code reproduces neither the experimental wavelengths of the 4–4 structures nor their intensity.

The experimental X-ray spectrum recorded for xenon at 4 bar and 350 J is compared to A/T calculations in Fig. 6. The experimental X-ray spectrum shows that Xe^{27+} and Xe^{28+} are the main ion stage emitting, in contradiction with the value of $Z = 24.3$ given by TS, which also yields $T_e = 390 \pm 40 \text{ eV}$, and $n_e = (1.2 \pm 0.5) \times 10^{20} \text{ cm}^{-3}$. However, for an A/T calculation to generate the Xe^{26+} ionic species, which dominates the spectrum, requires a T_e of 600 eV. For all the recorded X-ray spectra, the ionization measured by TS seems to be systematically lower than that inferred from the ion stages observed in the spectra. We can also observe in Fig. 6 that the quite strong sensitivity of the calculated spectra on the electronic temperature allows a precision better than 10% on the best fit temperature value.

In Fig. 7, we show the XUV spectra at different times obtained on Kr, at 4 bar and 230 J compared with the A/T calculations. For the early times there is quite good agreement for the short wavelengths, whereas for later times the agreement is better on the long wavelength side. For the X-ray emission,

Fig. 8, the theoretical fit is complicated by the inaccurate treatment of the optical depth of the Ne-like lines. The figure shows that the 6.5–7 Å region is well reproduced by the code, whereas for the shorter wavelengths the reabsorption is slightly underestimated, and it is overestimated for the longer wavelength region. As the spectrum has been calculated with the SOSA formalism, this disagreement could be due to a poor treatment of the coupling between the populations

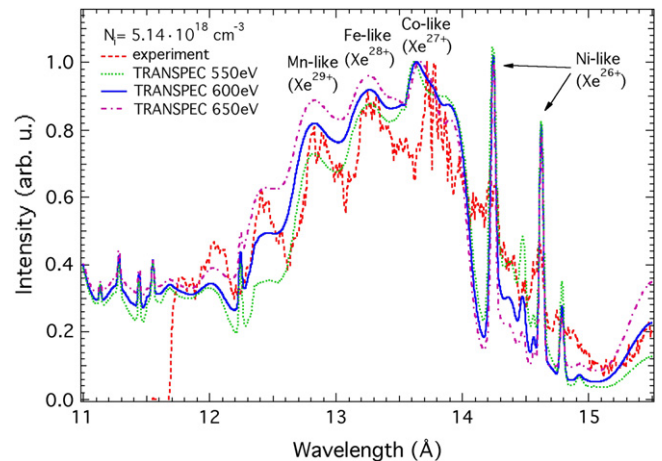


Fig. 6. Xenon X-ray spectrum recorded for 4 bar gas pressure and 350 J laser energy, compared with AVERROES/TRANSPEC calculations for 550 eV, 600 eV and 650 eV electronic temperatures ($N_i = 5.14 \times 10^{18} \text{ cm}^{-3}$).

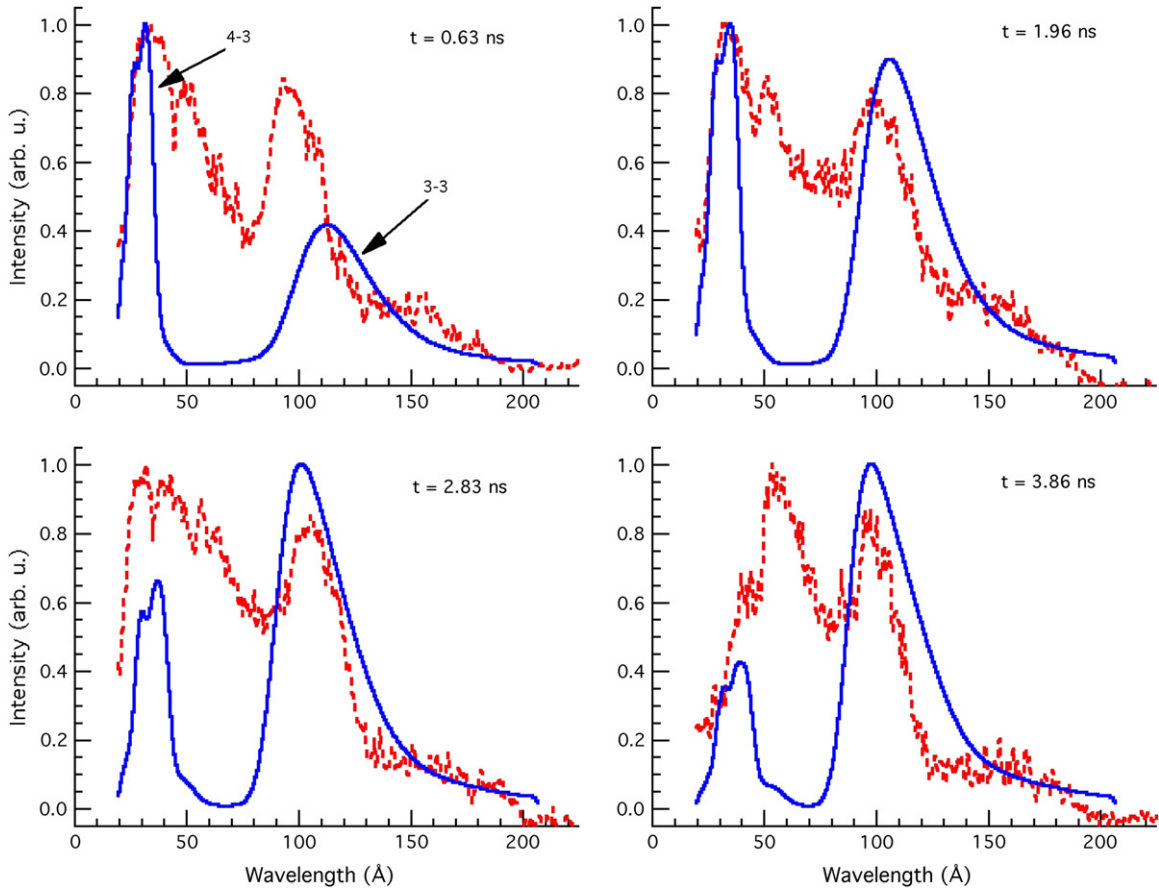


Fig. 7. Krypton XUV spectra at different times during the plasma evolution, for 4 bar gas pressure and 230 J laser energy (dashed lines). The AVERROES calculations (full lines) are performed using the TS deduced plasma parameters ($N_i = 5.12 \times 10^{18} \text{ cm}^{-3}$, $T_e = 170 \text{ eV}$, and $Z = 23$).

and the radiation, which cannot be accurately treated within the SOSA approach. The use of a Detailed Level Accounting (DLA) approach coupled to a proper treatment of line transfer [17] might provide better results. It has to be stressed that, as in the case of Xe, the X-ray spectrum has been calculated

using a temperature value (500 eV) higher than that measured with the TS diagnostic (170 eV).

5. Discussion

A first step to improve the agreement between calculated and measured XUV spectra consists of using a hydrodynamic code to obtain a more accurate description of the plasma parameter evolution as a function of time. The difficulty is the 3D character of the irradiation geometry. However, as a start, we have performed 1D simulations using the MULTI hydrocode [18]. In Fig. 9 we show the temperature profile as a function of time obtained with MULTI in the case of Xe, at 2 bar and 355 J, compared to the profile used to obtain the previous analysis shown in Fig. 5.

Fig. 10 shows the spectra obtained using the MULTI temperature profile in the TRANSPEC calculations, compared to the previous calculations. The width of the short wavelength structure and the shift of the long wavelength structure towards slightly shorter wavelengths yield better agreement with the experimental data. This provides encouragement to use 2D or 3D hydrodynamic simulations of the plasma.

The disagreement between the observed X-ray emission and the TS Z requires discussion. A first hypothesis to explain the discrepancy is that the homogeneity of the plasma is not

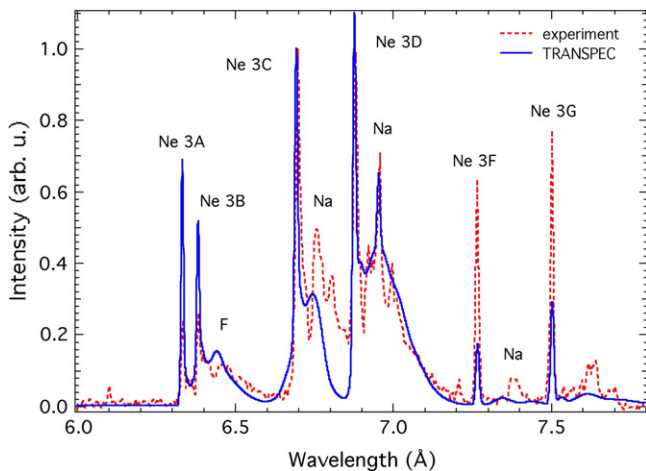


Fig. 8. Krypton X-ray spectrum recorded on the same shot than the XUV spectra in Fig. 7 (4 bar, 230 J), compared with AVERROES/TRANSPEC calculations for $N_i = 5.12 \times 10^{18} \text{ cm}^{-3}$ and $T_e = 500 \text{ eV}$.

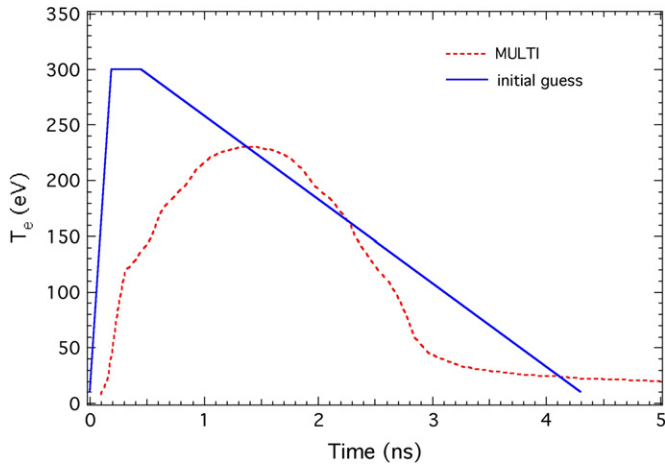


Fig. 9. Temperature profile issued from the MULTI simulation for the case of xenon, at 2 bar pressure, irradiated with 355 J laser energy, compared to the temperature profile used in the simulations of Fig. 5.

achieved in the experiment. The far-field intensity distribution of an RPP has, in general, an intensity envelope, which is essentially an Airy function, superimposed to a fine speckle pattern [19]. If this intensity pattern impinges on a solid target, the thermal conduction is sufficiently high to smooth the intensity of the speckle pattern. On the other hand, for a gas target the thermal conduction may be too small to obtain such

a smoothing [20]. In this case, the plasma behaves like a “bath” with given average electron temperature and density, with hot spots, generated by the speckles of the RPP. In this case, the XUV radiation, which is emitted by the whole plasma, is representative of a lower average temperature than the X-ray keV radiation, which is emitted only by the hot spots. If this hypothesis is correct, then the agreement between the XUV and the TS diagnostics could be due to the relatively large plasma region investigated by the TS diagnostic. The large widths of the TS satellites could confirm this scenario.

6. Conclusions and future work

Xenon and krypton X-ray and XUV spectra were recorded to benchmark atomic physics codes such as AVERROES in non-LTE conditions. Electronic and ionic Thomson scattering provided the measurement of electron and ion density, electron temperature and average ionization. An XUV streak camera was operated for gas pressures lower than 10 bar, using a differential pumping system. The dependence of spectra on laser intensity and gas pressure is in general agreement with the laser heating conditions of the gas jet.

Our data clearly show that the XUV emission vary in time, so the time resolution for this diagnostic is necessary. The spectra show that the ionization increases with pressure and

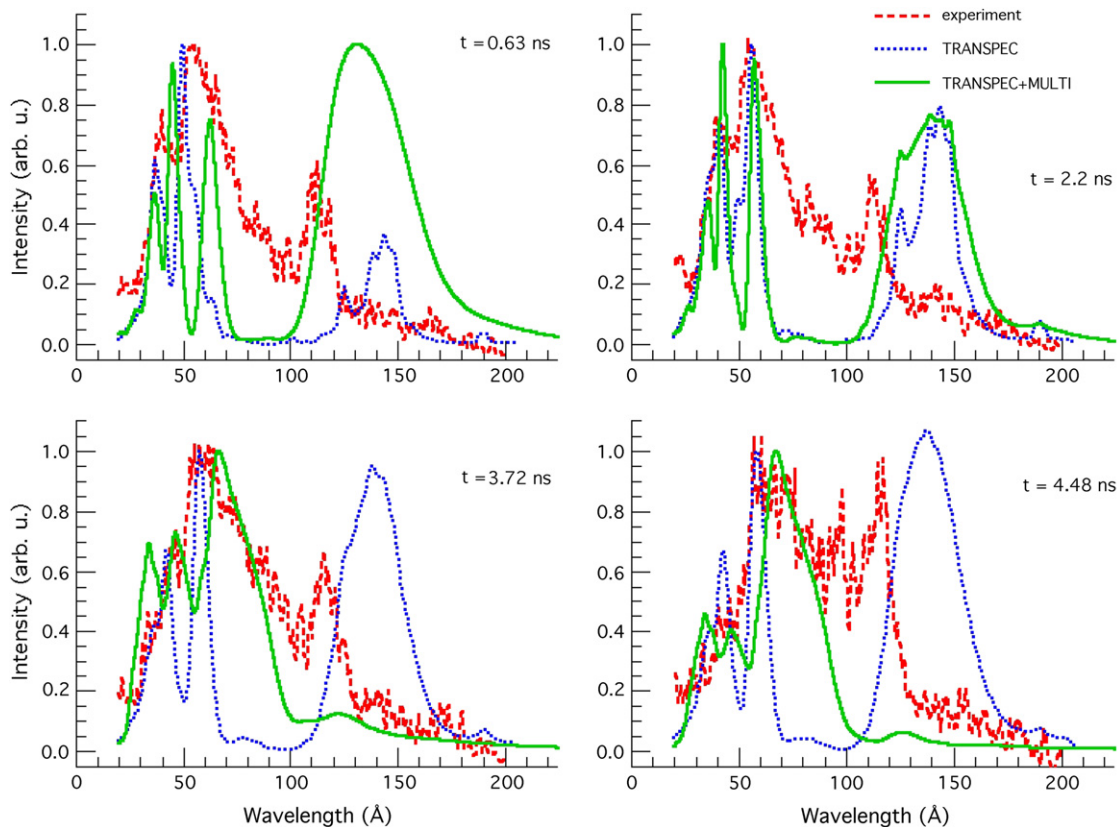


Fig. 10. Xenon XUV spectra measured for 2 bar gas pressure and 355 J laser energy (dashed lines) compared with the AVERROES/TRANSPEC calculations (full lines) performed using the MULTI temperature profile of Fig. 9. To the sake of a better comparison, the figure shows again (dotted lines) the same A/T calculations of Fig. 5.

laser intensity. To minimize the gradients and the cold gas re-absorption in the jet we have used an RPP to give an elliptical focal spot that match the gas jet cross-section. The use of this RPP may have introduced unwanted inhomogeneities in the laser focal spot that complicate the data interpretation. We noticed that by performing simulations with detailed and/or hybrid codes for the case of the Kr X-ray emission an improved treatment of the Ne-like lines could be obtained, if the coupling between the radiation and the level populations is taken into account.

Finally, we plan to perform 2D simulations, including the laser beam smoothing, with the aim of analyzing the homogeneity of the plasma, to get a better insight on the present disagreement between the X-ray data and the XUV and TS diagnostics.

References

- [1] C. Bowen, A. Decoster, C.J. Fontes, K.B. Fournier, O. Peyrusse, Yu. Ralchenko, *J. Quant. Spectrosc. Radiat. Transfer* 81 (2003) 71.
- [2] C. Bowen, R.W. Lee, Yu. Ralchenko, *J. Quant. Spectrosc. Radiat. Transfer* 99 (2006) 102.
- [3] J. Abdallah, R.E.H. Clark, D.P. Kilcrease, G. Csanak, C.J. Fontes, Various applications of atomic physics and kinetics codes to plasma modeling, in: A.L. Osterheld, W.H. Goldstein (Eds.), *Atomic Processes in Plasma. Proceedings of the Tenth Topical Conference, San Francisco, CA, AIP Conference Proceedings*, vol. 381, AIP, NY, 1996.
- [4] A. Bar-Shalom, J. Oreg, M. Klapisch, *Phys. Rev. E* 56 (1997) R70.
- [5] O. Peyrusse, *J. Phys B* 33 (2000) 4303; O. Peyrusse, *J. Quant. Spectrosc. Radiat. Transfer* 71 (2001) 571.
- [6] J. Bauche, C. Bauche-Arnoult, M. Klapisch, *Advanc. Atom. Mol. Phys.* 23 (1987) 131.
- [7] A. Bar-Shalom, J. Oreg, W.H. Goldstein, D. Sharts, A. Zigler, *Phys. Rev. A* 40 (1989) 3183.
- [8] S. Mazevet, J. Abdallah, *J. Phys. B* 39 (2006) 3419.
- [9] S.B. Hansen, J. Bauche, C. Bauche-Arnoult, M.F. Gu, *High Energy Density Phys.* 3 (2007) 109.
- [10] B. La Fontaine, H.A. Baldis, D.M. Villeneuve, J. Dunn, G.D. Enright, J.C. Kieffer, H. Pépin, M.D. Rosen, D.L. Matthews, S. Maxon, *Phys. Plasmas* 1 (1994) 2329.
- [11] S.H. Glenzer, K.B. Fournier, C. Decker, B.A. Hammel, R.W. Lee, L. Lours, B.J. MacGowan, A.L. Osterheld, *Phys. Rev. E* 62 (2000) 2728.
- [12] C. Chenais-Popovics, V. Malka, J.-C. Gauthier, S. Gary, O. Peyrusse, M. Rabec-Le-Gloahec, I. Matsushima, C. Bauche-Arnoult, A. Bachelier, J. Bauche, *Phys. Rev. E* 65 (2002) 046418.
- [13] V. Nagels, C. Chenais-Popovics, O. Peyrusse, S. Gary, F. Girard, V. Malka, M. Rabec-Le-Gloahec, J.-C. Gauthier, *Europhysics Conf. Abstracts* 28G (2004) 4.230.
- [14] J. Bauche, C. Bauche-Arnoult, O. Peyrusse, A. Bachelier, K.B. Fournier, C. Chenais-Popovics, J.-C. Gauthier, *J. Quant. Spectrosc. Radiat. Transfer* 81 (2003) 47.
- [15] V. Nagels, C. Chenais-Popovics, V. Malka, J.-C. Gauthier, A. Bachelier, J.-F. Wyart, *Phys. Scripta* 68 (2003) 233.
- [16] E.E. Salpeter, *Phys. Rev.* 120 (1960) 1528.
- [17] O. Peyrusse, *Phys. Fluids B* 4 (1992) 2007.
- [18] R. Ramis, R. Schmalz, R. Meyer-Ter-Vehn, *Comput. Phys. Commun.* 49 (1988) 475.
- [19] J. Garnier, *Phys. Plasmas* 6 (1999) 1601.
- [20] J.-R. Marquès, private communication.